iScience

Article

Continuous tremor monitoring in Parkinson's disease: A wristwatch-inspired triboelectric sensor approach

Graphical abstract

Highlights

- Developed a wristwatch-like PD tremor sensor (WW-TES) inspired by automatic watches
- Optimized electrode spacing for enhanced signal distinction
- Proposed a working mechanism aligning with WW-TES output signals
- Signal amplitude correlates with tremor severity levels in tests

Authors

Sirinya Ukasi, Satana Pongampai, Basanta Kumar Panigrahi, ..., Hoe Joon Kim, Naratip Vittayakorn, Thitirat Charoonsuk

Correspondence

naratip.vi@kmitl.ac.th (N.V.), thitiratc@g.swu.ac.th (T.C.)

In brief

Health sciences; Natural sciences; Materials science

Ukasi et al., 2024, iScience *27*, 111480
December 20, 2024
https://doi.org/10.1016/j.isci.2024.111480

CellPress

iScience

CellPress
OPEN ACCESS

Article

Continuous tremor monitoring in Parkinson's disease: A wristwatch-inspired triboelectric sensor approach

Sirinya Ukasi,[1,6] Satana Pongampai,[2,6] Basanta Kumar Panigrahi,[3] Swati Panda,[4] Sugato Hajra,[4] Hoe Joon Kim,[4] Naratip Vittayakorn,[5,6,7,*] and Thitirat Charoonsuk[1,6,*]

[1]Department of Materials Science, Faculty of Science, Srinakharinwirot University, Sukhumvit 23, Watthana, Bangkok 10110, Thailand
[2]Department of Physics, Faculty of Science, King Mongkut's University of Technology Thonburi, Bangkok 10140, Thailand
[3]Department of Electrical Engineering, Siksha O Anusandhan University, Bhubaneswar 751030, India
[4]Department of Robotics and Mechatronics Engineering, Daegu Gyeongbuk Institute of Science and Technology, Daegu 42988, South Korea
[5]Department of Chemistry, School of Science, King Mongkut's Institute of Technology Ladkrabang, Bangkok 10520, Thailand
[6]Advanced Materials Research Unit, School of Science, King Mongkut's Institute of Technology Ladkrabang, Bangkok 10520, Thailand
[7]Lead contact
*Correspondence: naratip.vi@kmitl.ac.th (N.V.), thitiratc@g.swu.ac.th (T.C.)
https://doi.org/10.1016/j.isci.2024.111480

SUMMARY

Parkinson's disease (PD) prevalence is projected to reach 12 million by 2040. Wearable sensors offer a promising approach for comfortable, continuous tremor monitoring to optimize treatment strategies. Here, we present a wristwatch-like triboelectric sensor (WW-TES) inspired by automatic watches for unobtrusive PD tremor assessment. The WW-TES utilizes a free-standing design with a surface-modified polytetrafluoroethylene (PTFE) film and a stainless-steel rotor within a biocompatible polylactic acid (PLA) package. Electrode distance is optimized to maximize the output signal. We propose and discuss the WW-TES working mechanism. The final design is validated for activities of daily living (ADLs), with varying signal amplitudes corresponding to tremor severity levels ("normal" to "severe") based on MDS-UPDRS tremor frequency. Wavelet packet transform (WPT) is employed for signal analysis during ADLs. The WW-TES demonstrates the potential for continuous tremor monitoring, offering an accurate screening of severity and comfortable, unobtrusive wearability.

INTRODUCTION

Parkinson's disease (PD), a neurodegenerative disorder manifesting itself through various motor symptoms, is estimated to affect over 12 million patients in 2040, as reported by the World Health Organization (WHO).[1] These symptoms, including involuntary movements, stiffness, and tremors, significantly affect daily functioning and progressively diminish quality of life in patients. Even though medications can help maintain the PD severity, long-term taking or maximum dose of medication can lead to side effects, particularly dyskinesia.[2] Medicine adjustments are frequently required by clinicians to assign appropriate doses. Nevertheless, the accuracy of symptom presentation is worrying. Sometimes, patients do not show immediate symptoms in in-person treatment, but it happens during the day before or after. Finding innovative technology to help patients and clinicians comfortably monitor PD severity is necessary for effective care and treatment. Wearable sensors (WS) have been known in the field of health monitoring technology in the past decades and also gained much attention for emerging as monitoring devices for PD symptoms.[3,4] These tools allow patients with PD and clinicians to autonomously monitor and understand the relationship between physical activity and the level of symptom severity. The most common uses include inertial sensors such as accelerometers (ACC) and gyroscopes (GYRO),[5] as well as biopotentials such as electromyography (EMG).[6] Prior studies have utilized these sensors to monitor the motor and non-motor symptoms of PD, such as shuffling steps, sudden movement changes, and abnormal shaking in patients. However, traditional WS used for PD monitoring often face challenges such as invasiveness, restricted movement, user discomfort, potential interference with measured movements, and reliance on batteries, which limit the continuous monitoring of device, in addition to heavy and bulky size. Therefore, it is necessary to address these challenges by developing a new type of PD sensor that can carry the patient and provide functional measures that are associated with quality of life.

Among the cutting-edge technologies contributing to this field, triboelectric sensors (TES) have opened up a vast market for sensing systems through the capability of contact electrification and electrostatic induction of two distinct materials to generate electrical signals.[7,8] The TES device also shows substantial potential as WS due to its excellent performance in harnessing mechanical energies at low frequencies (<5Hz),[9,10] which means that the motion of humans with PD can be potentially detected. Moreover, the structures and materials can be easily designed to adapt to WS applications.[11–13] To date, numerous TES

structures have been designed and proposed for applications in physical detection and the monitoring of human activities.[14–16] The versatility of TES has enabled its utilization across various domains, including sports and fitness,[17] where it facilitates physical activity tracking, and healthcare,[18] where it is employed in health monitoring.[19,20] The application of TES in these fields is driven by its capacity to provide real-time, non-invasive data, thereby offering significant benefits for continuous monitoring and proactive health management.[21,22]

According to the literature, previous studies have also attempted to examine the use of TES for assessment in different structures. The sock-based TES was developed in 2019 by coating fabric with PEDOT: PSS and embedding it with lead zirconate titanate (PZT) chips for PD gait analysis.[23] However, the use of PZT ceramic raises concerns due to its brittleness and toxicity, making it difficult to utilize WS. A design of waterwheel-like TES was proposed; unfortunately, a low signal-to-noise ratio of electrical output was generated from this kind of TES, making it difficult to distinguish small signal amplitudes from ambient noise.[24] A stretchable TES was designed in another work based on Ecoflex and aluminum to measure muscle movements of patients with PD for insights into disease progression. Nevertheless, challenges persist due to the difficulty of accurately placing sensors on specific tendons. Variations in fat and tissue also limit the ability of sensor to measure muscle activity.[25] The M-shaped TES for tremor detection was developed utilizing hydrogel of catechol, chitosan, and diatom.[26] Although the electrical signal information about tremor amplitude and patterns can be achieved, the challenges still remain, especially unsuitable device structures for body attachment. In developing the TES device, other than the significance of the signal, it is very important to consider the convenience of the patient to carry and wear so as not to feel heavy and bulky during activity. This is because the patient must wear it all the time. Therefore, there is a desire to develop TES further with important features of a high signal-to-noise ratio, a lightweight structure, and comfort to wear. To achieve the goal, a well-designed structure must consider crucial parameters such as material selection[27] and modification,[28,29] suitable operating mode selection,[30] and appropriate structural design.[31]

Herein, a custom-designed wristwatch-like triboelectric sensor (WW-TES) is proposed to be a wrist-worn sensor for PD tremors monitoring. The development process involved designing a free-standing (FS) mode TES using stainless-steel and surface-modified PTFE as the triboelectric pair. The basic structure of regular FS devices was fabricated firstly to observe the electrical output characteristics, including open circuit output voltage (V_{OC}) and short circuit output current (I_{SC}) in relation to the surface-modified PTFE, electrode distance, and frequency to find the possibility for further designing of WW-TES device. The optimized WW-TES device's structure is tested with various frequencies. The practical application for PD tremor monitoring was validated through activities of daily living (ADLs), which included tasks such as pouring water and eating based on the MDS-UPDRS scale. The digital signal process technique was performed to understand the signal during activities. This proposed WW-TES shows the potential for screening tremor severity and provides the possibility to monitor the daily living conditions of patients continuously.

RESULTS AND DISCUSSIONS

Materials modification and electrical output performance based on free-standing mode triboelectric sensor

Based on the triboelectric mechanism involving contact electrification and electrostatic induction, selecting two distinct materials is essential. When two dissimilar materials come into contact, electrons are typically transferred from one material to the other according to their electronegativity (EN) differences. The amount of charge transferred correlates proportionally to the EN difference between the materials. In this work, PTFE film was selected as the tribonegative material due to its high electron affinity, which arises from fluorine atoms (high EN) within its structure. Conversely, stainless steel was chosen as the tribopositive material for two main reasons: (1) its relatively low EN, which facilitates electron donation, and (2) the design inspiration from automatic watches, specifically the WW-TES mechanism. Given that the operation of WW-TES was inspired by the rotational movement of an oscillating plate in a watch, the second-hand oscillating plate from the watch mechanism was selected for contact with the PTFE film. Therefore, stainless steel was utilized as the tribopositive contact material. This selection is further supported by material characterization results discussed in the WW-TES design and proposed mechanism section. For the material modification, the surface of PTFE was polished with sandpaper to enhance its output performance by increasing its surface roughness. The morphology and roughness of the modified PTFE film were analyzed using SEM and AFM. The SEM images in Figures 1A and 1B show significant changes in the surface morphology of the PTFE film before and after the surface modification. The images reveal a smooth surface of the pristine PTFE (Figure 1A) before the sandpaper treatment and a visibly roughened surface after the treatment. The use of sandpaper resulted in noticeable scratches with line structures on the surface (Figure 1B). Consistent patterns were observed in the ATR-IR spectra before and after polishing, as shown in Figure S1, despite visible physical changes. This indicates that the chemical structure of PTFE remained unchanged throughout the polishing process. The AFM results (Figures 1C and 1D) show the two- and three-dimensional topography (scan area 10 μm × 10 μm) of the surface before and after the roughening process. Figure S2 shows the extracted line profile contains the information related to roughness. The root means square roughness (Sq) value for unmodified PTFE was observed to be 45.4 nm and it was increased to 227.9 nm after modification. It was found by comparing the generating output of unmodified and modified PTFE that the V_{OC} and I_{SC} of modified PTFE was higher than the unmodified PTFE for ∼1.8 and ∼1.6 times, as shown in Figures 1E and 1F. The surface pattern was similar to those in previous research, where the tribomaterials underwent surface modification with polishing, which resulted in improved overall output performance. Hence, the modified PTFE surface was used in all experiments in this study.

The working principle of regular FS-TES is based on an in-plane charge separation mechanism. The device consists of a free-standing stainless-steel layer (2 × 2 cm^2) and two PTFE films (2 × 2 cm^2) attached with Al electrodes (2 × 2 cm^2). The

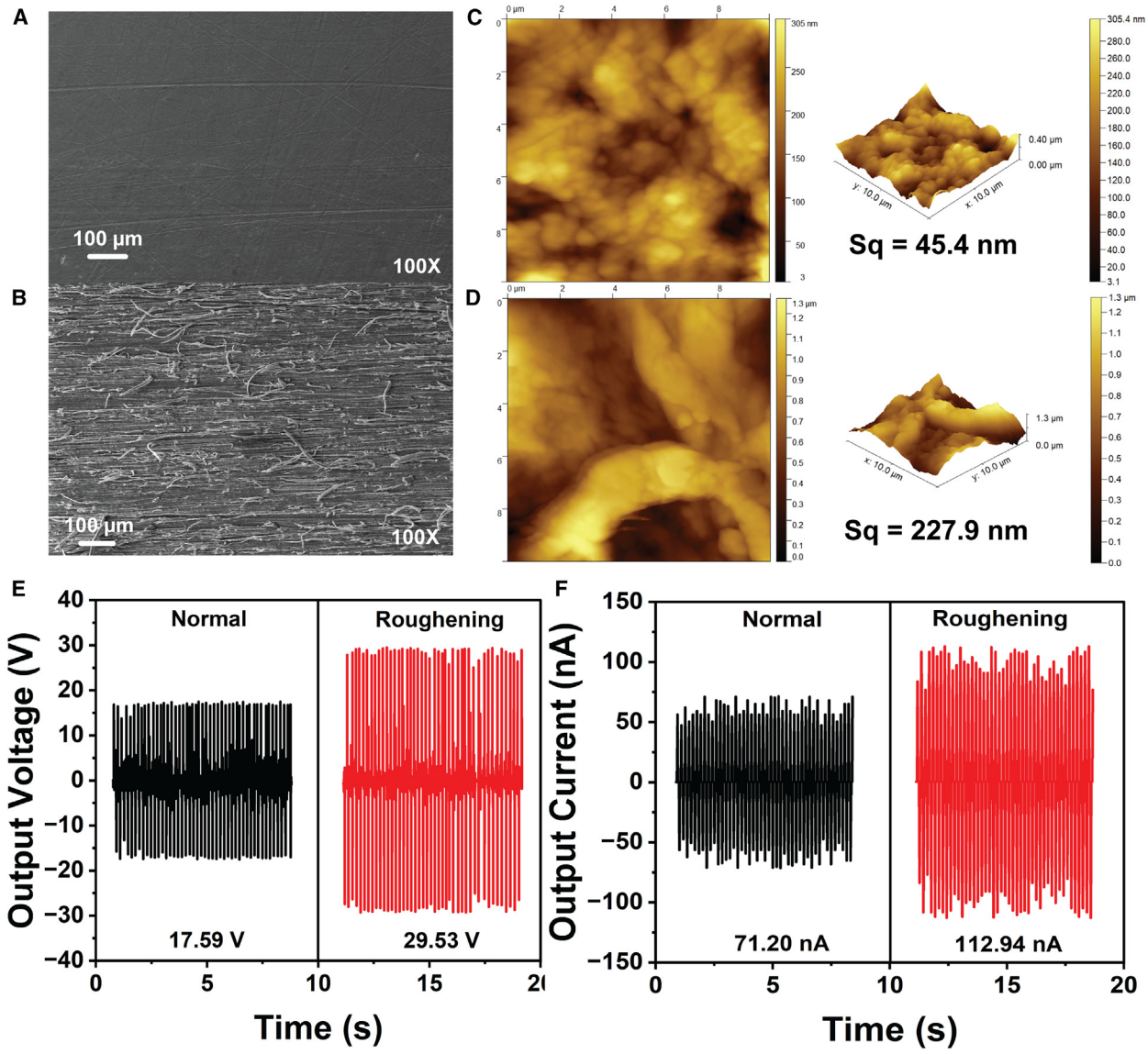

Figure 1. The surface characterization and electrical output of pristine PTFE and modified PTFE

(A and B) SEM images of pristine PTFE film (A), and modified PTFE film (B).

(C and D) AFM images showing the surface morphology of pristine PTFE film (C), and modified PTFE film (D).

(E and F) Electrical output V_{OC} (E), and I_{SC} (F) of the PTFE before and after surface modification by polishing.

stainless steel and two PTFE films are placed parallel to each other. The stainless steel is moved back and forth mechanically from one edge of the left-hand PTFE film to the end edge of the right-hand PTFE film. Meanwhile, the electrodes made of aluminum were attached to the bottom of the PTFE film and connected to the electrical wire, which was then connected to the load. In Figure 2A, SEM images are shown to demonstrate the FS-TES components. Arrows and symbols are added to represent the working principle. According to Figure 2A, during the initial state, a process known as charge exchange takes place between PTFE and stainless steel, which is caused by the difference in their electronegativity. However, the amount of electrostatic charge generated is equivalent to the continued contact of the materials. As a result, there is no difference in potential between the two electrodes, leading to the absence of any current flow in this state. When the stainless-steel layer partially contacts the PTFE film on the left electrode (LE), their different ability to attract electrons causes positive charges to be generated on the surface of the stainless-steel layer and negative charges to be generated on the surface of the PTFE layer. This is due to the triboelectrification effect following their physical contact. Upon the accumulation of negative charges on the PTFE film, an equal number of positive charges is induced in the LE. This induces an equal number of negative charges in the right-hand electrode (RE). This state can be seen according to the state (i) in Figure 2A. Further, under the

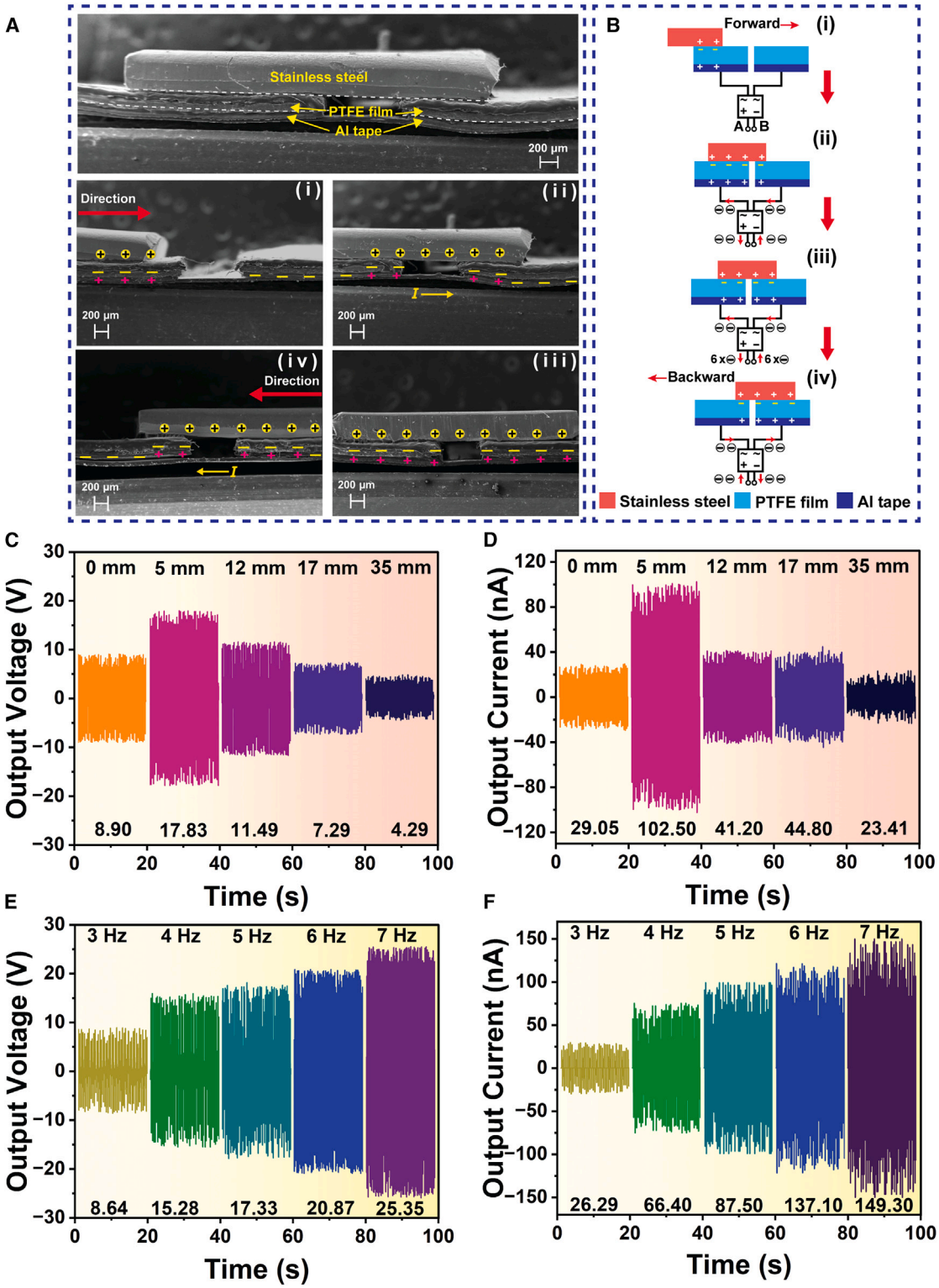

Figure 2. Working principle and electrical output of regular TES

(A) SEM images with a schematic diagram of the working principle.

(B) The figure depicting the working principle for FS-TES device.

(C) V_{OC} and I_{SC} of FS-TES by varying the distance of electrodes.(D and E) The electrical output V_{OC} (D) and I_{SC} (E) of FS-TES by varying frequency.

influence of the external force, the stainless steel starts to slide toward and overlap some parts of the RE while carrying the positive charge on the surface with it. The positive charges on the stainless-steel surface will induce the negative charges on the PTFE film on the RE. Consequently, some of the positive charges are induced on the RE, causing the previously formed electrons to flow through the load from the RE to the LE, producing an electric output at state (ii). During this sliding motion, electrons continue to flow between the two electrodes to balance the local potential until they reach the maximum output. This process contributes to the first half-cycle of the FS-TENG in the state (iii). The second half-cycle is obtained during the reverse sliding motion of the stainless steel from RE to LE, and electrons flow in the opposite direction at state (iv). Alternating contact separation between the PTFE with Al electrode and stainless steel is continued and prolonged, and an alternating current (AC) waveform is achieved. The drawing diagram of this working principle for FE-TES is also clearly shown in Figure 2B. In every contact-separation cycle, the total amount of the transferred charges (Q) is given by Equation 1:

$$Q = lab \quad \text{(Equation 1)}$$

where σ represents the surface triboelectric charge density on the PTFE's surface, while *a* and *b* are the length and width of the friction area and the effective range of the charge induction (*d*) was assumed to be constant in sliding and FS-mode TES. The potential difference can be described by Equation 2:[32]

$$V = \frac{-1}{C} \times Q + V_{OC} = -d_0 + \frac{g}{\varepsilon_0 S} \times Q + \frac{2\sigma x}{\varepsilon_0} \quad \text{(Equation 2)}$$

Where *V* is the potential difference between two metal electrodes, *C* stands for the capacitance, d_0 represents the initial gap distance between components in the nanogenerator, g signifies the gap distance between the electrodes, ε_0 represents the permittivity of free space, *S* is the area size of the effective surface, σ is the charge density and ϵ stands the permittivity of the material used in the free-standing layer. The relationship between charge generation and V_{OC}, where *S* is the area size of the effective electrode 1 and 2.[32]

$$V_{OC} = \frac{\Delta Q_{SC}.S}{C} \quad \text{(Equation 3)}$$

Continuing from the result in Figure 1, the enhancement of electrical output by increasing surface area can be described by the mathematics Equation 3 that the electrical output depends on *S*. Thus, improving the surface contact area can increase the total electrical output.[33] The generated current can be calculated as provided in Equation 4.

$$I = \frac{dQ}{dt} = \frac{\sigma ab}{d/v} = \frac{v\sigma ab}{d} \quad \text{(Equation 4)}$$

where d and υ denote the electrode distances and relative speed of contact separation. The I_{SC} refers to transfer charge as a function of sliding time, which can be written as Equation 5, which relies on the stainless-steel motion speed.[34,35]

$$I_{SC} = \frac{dQ_{SC}}{dt} = \frac{dQ_{SC}}{dx}\frac{dx}{dt} = \frac{dQ_{SC}}{dx}v \quad \text{(Equation 5)}$$

Herein, the basic structure FS-TES was fabricated firstly to explore key parameters affecting its electrical performance. One of the crucial parameters is the distance between the two electrodes, which dictates the sliding displacement affecting electricity generation. The characteristics of V_{OC} and I_{SC} were examined by considering various electrode distances of 0, 5, 12, 17, and 35 mm to determine the optimal distance for achieving the maximum electrical output. It could be observed in Figures 2C and 2D that the output signals of V_{OC} and I_{SC} at 0 mm distance are 8.9 V and 29.0 nA. Upon increasing the electrode distance to 5 mm, a substantial rise in the output signal was observed, with V_{OC} and I_{SC} reaching 17.8 V and 102.5 nA. However, when the electrode distance exceeded 5 mm to be 12, 17, and 35 mm, there was a significant decrease in the electrical signal values. At this point, the electrode distance has less influence on the output. The output signal decreases to a certain extent with the increase in electrode spacing. According to Equation 3, by considering Δ Q_{SC} and S as constant, and V_{OC} is proportional to C. Normally, dividing the gap between electrodes into smaller segments will significantly increase C, resulting in a lower V_{OC}. Thus, in this case, the large distance between electrodes can effectively decrease the C value to get a higher V_{OC}. It can be seen that the output signal increases as the distance between the electrodes increases from 0 mm to 5 mm. However, there is an optimum gap that generates the largest output. Beyond this optimum point, the output signal value starts to drop due to the breakdown effect that basically induces the loss of the electrostatic energy. The breakdown effect leading to the loss of electrostatic energy in an FS-TENG can be represented by Paschen's Law. Paschen's Law provides a relationship between the breakdown voltage, the pressure of the gas medium, and the distance between the electrodes. It is expressed as Equation 6:[36]

$$V_b = \frac{apd}{ln(pd)} + b \quad \text{(Equation 6)}$$

where: V_b is the breakdown voltage, d is the distance between the electrodes, p is the pressure of the gas medium, b is a constant depending on the gas medium, and a is another constant related to the specific gas. The breakdown effect for FS-TENG can be considered in two possible ways: one occurs between two electrodes, and the other occurs between the triboelectric surfaces and an electrode.[37] The breakdown effect can be formed once the V_{OC} is high enough to cause a discharge spark and generate the breakdown channel between electrodes, causing the obvious release of voltage and charge dissipation. Meanwhile, another breakdown threshold can be formed across the dielectric layer and bottom electrodes that can be determined directly by dielectric strength multiplied by its thickness. The gap distance between the electrodes has a significant effect on the breakdown threshold. As the gap increases, the breakdown threshold increases, resulting in a decrease in output

performance. Similar to the work of W.-Z. Song et al.,[38] where the influence of electrode spacing on the output of DC-triboelectricity was also found. Various studies have also reported the significance of the breakdown effect affecting the output performance of electricity generation.[36,39] Therefore, in this work, a gap of 5 mm between the electrodes was determined to be the optimal distance. The purpose of this work is to create a sensor that can be worn on the wrist to monitor Parkinson's disease. Frequency sensitivity is a crucial factor to consider in the design process. The frequency variation can directly impact the amplitude of output generation, so the FS-TES device was tested with an electrode distance of 5 mm. Systematic output measurements were taken within the frequency range of 3–7 Hz Figures 2E and 2F demonstrate the output signals of V_{OC} and I_{SC} when measuring at 3 Hz, generating 8.64 V and 26.29 nA. As the frequency increased from 3 to 7 Hz, the output signal progressively increased, reaching a maximum of approximately 25.35 V and 149.30 nA at 7 Hz. It is clear that the output signal of both V_{OC} and I_{SC} is directly proportional to the increased frequency, due to the increased speed. This shortens the duration of one working cycle and increases the number of working cycles in a given time. As a result, surface charge can be generated on the surface with higher density before transferring to an external load, resulting in an overall increase in total output. This demonstrates that the device can operate at various frequencies and the output generated is related to the frequency.

The components of the WW-TES device can be divided into three main parts, including (1) the device frame or package, (2) the triboelectric material pair, and (3) the stainless-steel rotor plate as shown in Figure 3A. Some details need to be gently created on the device frame, i.e., holes and rotor plate substrate for smooth attaching the materials pair before adding with the watch strap. The expected design for the final WW-TES device is displayed in Figure 3B. The experimental steps of device fabrication were separated into two parts of frame fabrication and WW-TES device assembly, according to the schematic diagram of the experiment in Figures 3C and 3D. As illustrated in Figure 3C (i), the designed frame was done with the Shapr3D software (Shapr3D App Version 5.572.6640.0) to create exact shape and size of the frame and all required components, such as holes and substrate for material pair attaching. The 3D model files were imported into software of ideamaker (ideasMaker 4.3.2 Raise3D E2) to slice and obtain the gcode files. Subsequently, the frame was 3D printed using PLA filament on a Raise3D printer (Fused Deposition Modeling printer; FDM) with a resolution of 0.2 mm. The printing temperature of 210°C and printing speed of 60 mm s^{-1} were used. The frame of the device was designed to be similar to the shape of a round watch case with specific dimensions: 2 mm width, 7 mm height, and a diameter of 34 mm. The frame featured a platform in the center and two inward extensions for the placement of the rotor plate and PTFE. A visual representation of the device frame fabrication process can be found in Figure 3C (ii). The schematic diagram of assembly steps for the designed WW-TES is displayed in Figure 3D. Initially, a surface-modified PTFE (10 × 0.5 mm^2) is affixed with aluminum tape (10 × 0.5 mm^2) as the electrode and connected to electrical wires (step (i)). This assembly is then adhered to one of the inward extensions, with the electrical wires routed out through the side hole according to the step (ii). The same procedure is repeated for the other inward extension. The stainless-steel rotor plate is then secured to the central section of the device as can be seen in step number (iii). A nut and metal bearing, serving as the proof mass with a total weight of 3.32 g, are affixed to the rotor plate to help smooth the rotation of stainless-steel during operation. This is consistent with the step (iv). After assembling the WW-TES device in part of the WW-TES face, the next step was to attach it with a watch strap so that it could be worn on the wrist like a watch. Finally, the final WW-TES device was obtained as can be seen in step (v). The total weight of the device is 33.49 g, which is lighter than that of a regular automatic watch.

Proposed working mechanism and electrical output performance of the wristwatch-like triboelectric sensor

The WW-TES was designed based on the mechanism of an automatic watch, aiming for patients to be easier to carry in case of required monitor of Parkinson's symptoms at home. Automatic watches are known for their reliability and long-lasting mechanisms as long as the wearer keeps moving. They can also generate energy from the irregular and chaotic movements of the wrist.[40] An automatic watch movement features a freely rotating metal weight called the rotor plate. The movement from the wrist causes the rotor plate to rotate and spin. As it spins, it automatically coils the mainspring inside, providing power for the watch. Given the significance of the rotor plate that can be moved freely to make the automatic watch work, the attention in this work was then paid to utilizing it to develop a WW-TES. Therefore, the watch parts of the rotor plate were bought to fabricate the WW-TES with a custom design. Before using it, characterization was done to confirm the type and composition of the material. The EDS mapping technique was employed as depicted in Figure S3; the results revealed the presence of elements consistent with stainless steel, including C, O, Si, P, S, Cr, Fe, and Ni by reporting its composition detailed in Table S1. These findings are in accordance with prior research references[41,42].

According to the structure of the WW-TES, there is a rotor plate made of stainless steel, which serves as the tribo-positive material. It is attached at the center of the frame with a nut and bolt, acting as the proof mass for smooth rotation. The two PTFE films serve as the tribo-negative material, affixed to aluminum electrodes. These electrodes are positioned within the frame and connected to electrical wires that extend outside of the frame. Figure 4A illustrates the 3 main steps of a stainless-steel rotor plate movement inside the WW-TES. The stainless-steel plate touches the first electrode during the period of stated rotation, further touches both electrodes in the intermediate state, and finally rotates to complete the cycle at the end of the loop. This rotation was filmed by a digital camera in slow-motion mode to match the observed electrical signal for tracking the AC electricity generation mechanism. The mechanism of electrical output generation from the WW-TES device is proposed. The schematic diagram was written to clearly describe, as shown in Figure 4B, by extracting it from the real V_{OC} signal. The proposed mechanism diagram illustrates the specific working principle of the WW-TES device, highlighting how the rotor plate undergoes rotation when exposed to an external force. As can be seen in

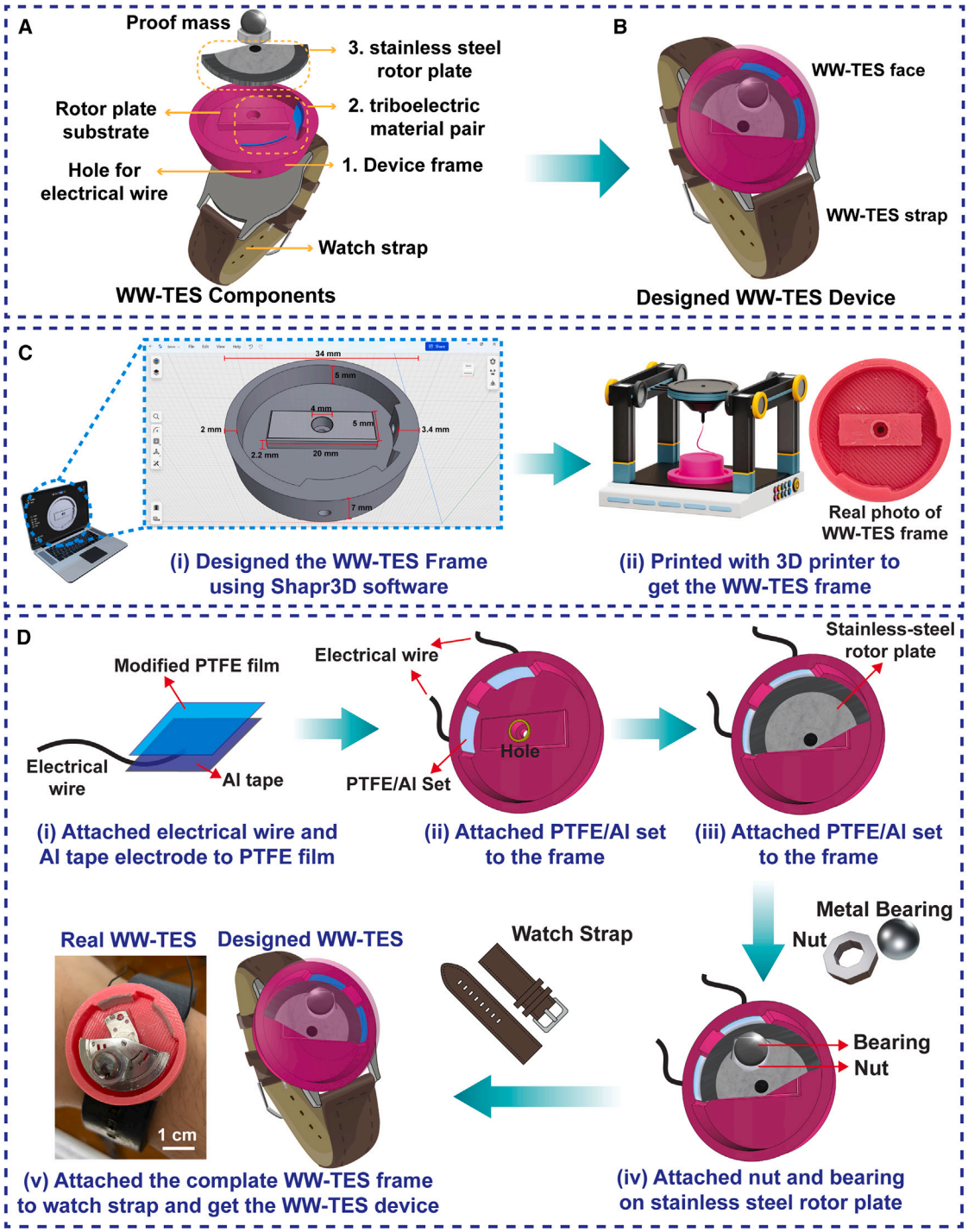

Figure 3. Design and fabrication process of WW-TES device

(A) The designed components.

(B) The target of the final WW-TES device with experimental fabrication steps.

(C) The fabrication of the device's frame using the 3D printing method.

(D) A schematic diagram of the WW-TES device assembly (the scale bar in step v is 1 cm).

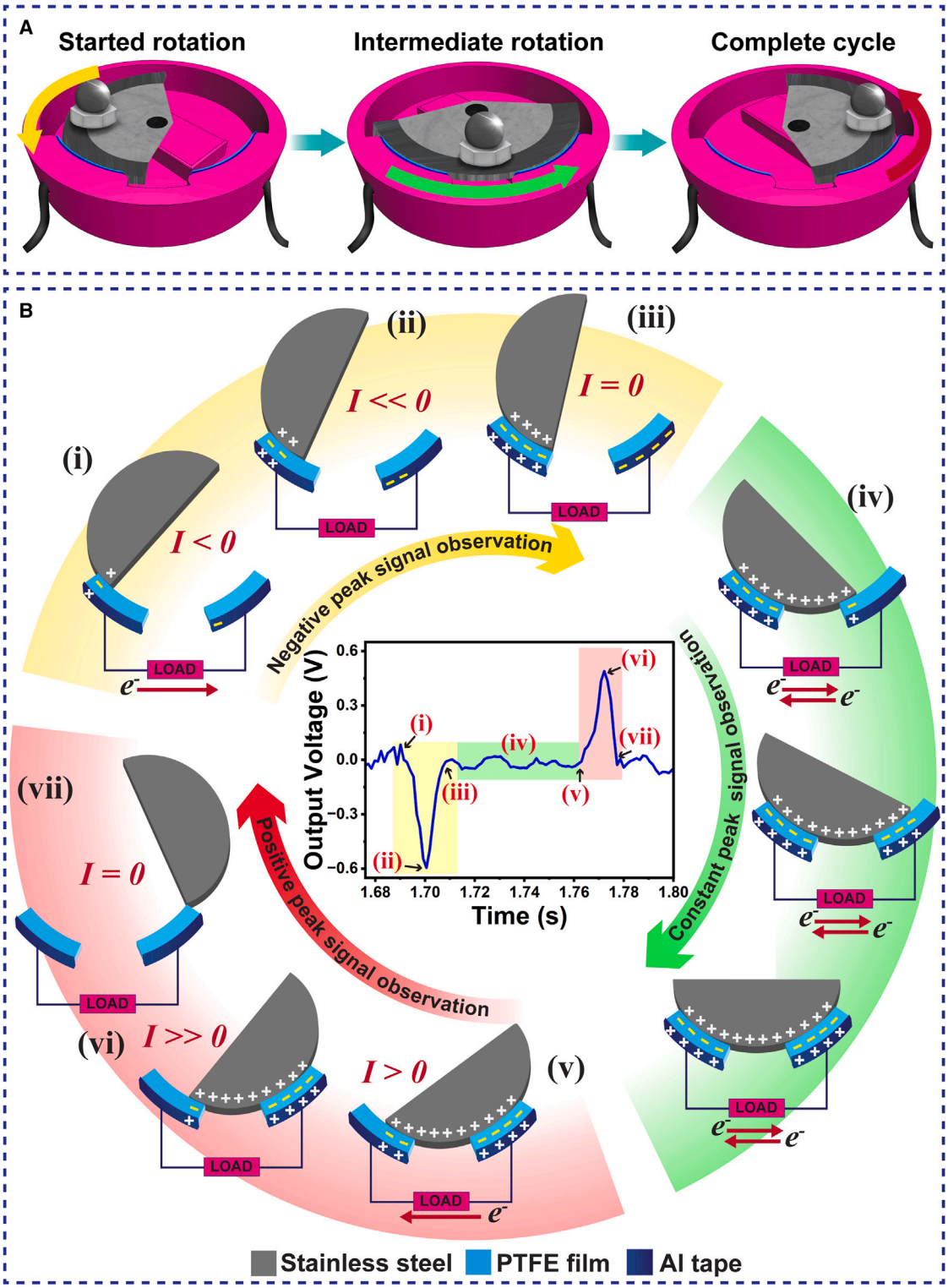

Figure 4. The working principle of the WW-TES device

(A) The steps of a stainless-steel rotor plate movement inside the WW-TES device.

(B) The working principle of the WW-TES device.

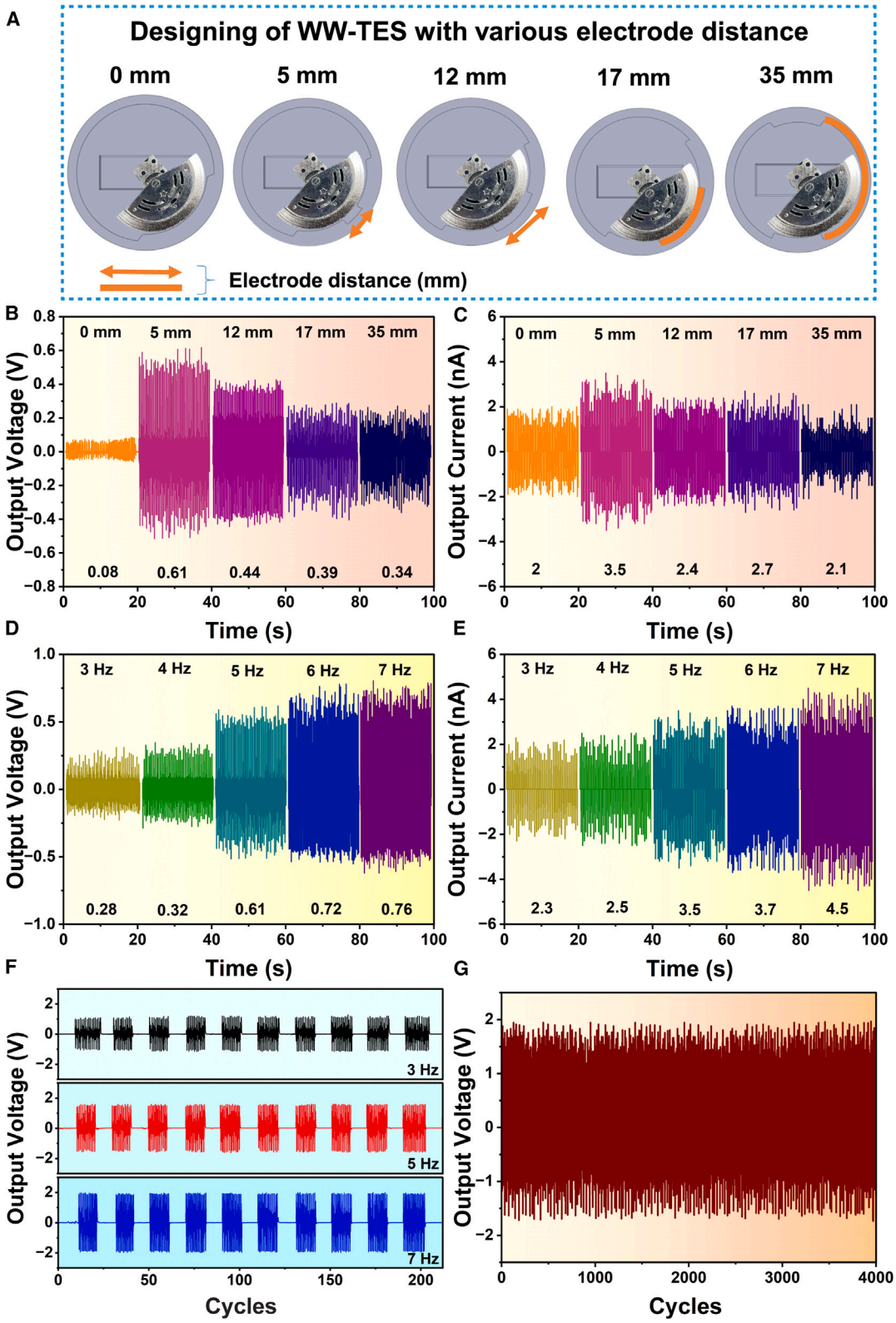

(legend on next page)

Figure 4B, the generating of the electrical output signal by WW-TES is separated into three main parts based on the real signal of an observed voltage of 1) negative peak signal observation (yellow region), 2) constant peak signal observation (orange region), and 3) positive signal observation (red region). The state of the mechanism to give a negative signal can be described in the 3 steps from (i) to (iii). The state when the rotor plate swings and contacts the PTFE film is defined as the first state of the mechanism (state (i)). The Intermolecular Electron Cloud Overlap Transfer (IECOT) model[43] is basically used to explain the distinct electron-donating and electron-receiving properties of materials. Metals typically tend to donate electrons, resulting in a positive charge on their surfaces. Conversely, PTFE sheets tend to attract electrons, leading to a negative charge on their surfaces. Because an Al tape is attached to the PTFE film, it undergoes induction from electrical neutrality to positive charges on the electrode. This induces a flow of electrons, causing them to move from the left-hand electrode to the right-hand electrode. However, since the stainless-steel rotor plate has started to touch PTFE, the current of induced I is small, resulting in signal $I < 0$. Upon prolonging time, the rotor plate continues to move, maintaining contact with the PTFE with more contact area, and undergoes continuous charge transfer until the maximum output on the negative side is obtained for $I << 0$, as illustrated at state (ii). The current flow continues until equilibrium is reached, which occurs when the rotor plate makes full overlap with the PTFE at state (iii). This induces an equal number of charges, causing no current to flow by giving signal $I \approx 0$. After that, the state (iv) of constant V takes place. During state (iv), the rotor plate reaches some part of the right-hand side electrode. The induced electron transfer between the rotor plate and the PTFE leads to the development of a negative charge on the surface of PTFE. Consequently, the Al electrode undergoes the induction of positive charges. At the same time, the rotor plate reaches an overlapping position of the two PTFE films and maintains contact with them throughout its movement. As a result, electrons flow back and forth between the two electrodes. At this stage, almost no electrical signals are generated. The next step of the mechanism is explained with state (v). The rotor plate continues to move away from the left-hand electrode, causing the charge imbalance to reappear. The electrons flow back in the opposite direction and move from the right-hand electrode to the left-hand electrode, starting to create the opposite direction with $I > 0$ of signal to give an alternative (AC) current. The flow of electric current continues until it reaches its maximum peak on the positive side at the state (vi). The I at this state is supposed to be $I \gg 0$. Then, the rotor plate continues to rotate to reach a point where it passes completely over both PTFE films, as can be seen in the state (vii). At this stage, there will be no current flowing again ($I \approx 0$), which is considered the end of the cycle. If there is a continuous external force, such as a tremor, this will cause the rotor plate to continue to rotate in the manner described above and produce an electrical signal.

To validate the WW-TES device for providing the highest efficiency, the output signals, including V_{OC} and I_{SC} with various electrode distances from 5 to 35 mm compared to 0 mm, were investigated. The adjusting of distance between electrodes was done at the beginning during the designed 3D printing of the frame before the assembly component of the device. The drawing diagram of designing WW-TES with various electrode distances is displayed in Figure 5A. The output signals were studied by using an orbital shaker as a vibration generator to excite the device. According to Figures 5B and 5C, the results show that the electrical output signal follows a similar trend to those observed in the basic FS-TES. At 5 mm, the device can provide the highest electrical output signal of both V_{OC} and I_{SC}, which is about 0.61 V and 3.5 nA. This result is truly evident that the electrode distance at 5 mm was the suitable parameter for constructing the WW-TES device in this work. After the optimization of electrode distance, the WW-TES was able to detect signals at various frequencies effectively. Basically, the high- and low-amplitude characteristics of tremors differ in different PD severity. The classic tremor associated with Parkinson's disease occurs at a frequency of 4–6 Hz and is characterized by a hand tremor that resembles the motion of rolling a pill between the fingers. Therefore, we further studied the device by measuring various input frequencies, as illustrated in Figures 5D and 5E. The output signal produced by the WW-TES demonstrated a proportional increase with the increasing input frequency. Notably, there is a direct correlation between the amplitude of the output signal and the tremor frequency. The characteristics of tremors in Parkinson's disease are classified into three types: rest tremor, postural tremor, and kinetic tremor. Rest tremor occurs when there is no voluntary muscle activity, while postural tremor occurs when holding head, arm, and leg motions against gravity. The specific frequency for postural tremor is 4–7 Hz. Kinetic tremors occur mostly at 7–12 or over.[44] The device used to measure these tremors was sensitive enough to detect various frequencies, even low ones. To test the stability of the device, it was subjected to vibration using an orbital shaker. According to the results in Figure 5F, the output signal of the device was stable at different frequencies, even when the device vibrated at 3 Hz for 10 s, followed by a 10-s pause. This cycle was repeated for 10 rounds. During the experiment, it was observed that the device produced output signals when it was vibrating and stopped producing output signals when it was not vibrating. Similarly, stable electrical values are obtained regardless of the vibration frequency, as shown by the results for both 5 Hz and 7 Hz. Additionally, when testing stability by allowing the device to operate continuously for 4000 s, it was observed that the device consistently detected tremors and maintained a stable electrical output throughout the experiment

Figure 5. The schematic diagram of designing WW-TES with various electrode distances and electrical output

(A) A design of WW-TES with various electrode distances.

(B and C) The electrical output V_{OC} (B) and I_{SC} (C) of the WW-TES device by varying the distance of electrodes.

(D and E) The electrical output V_{OC} (D) and I_{SC} (E) of the TES device by the frequency.

(F) The cycles of output signal stability.

(G) The stability continues for 4000 s.

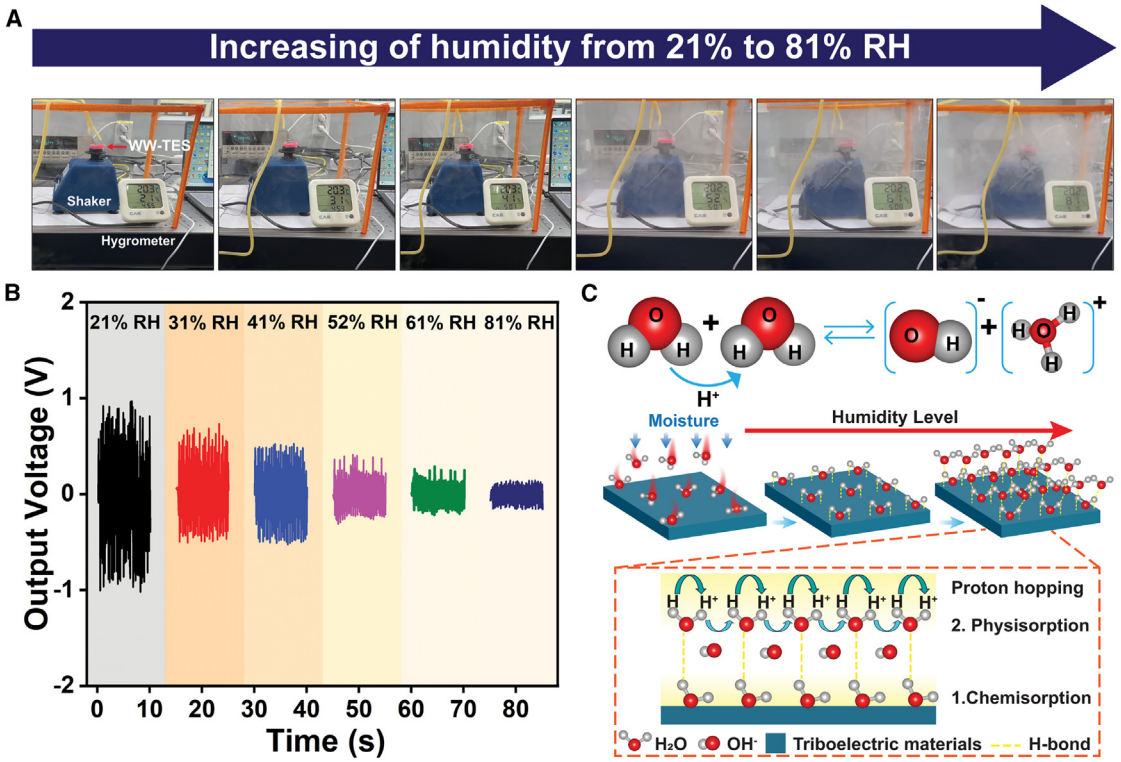

Figure 6. Humidity testing of WW-TES device

(A) The digital picture of the humidity setup and the operation of WW-TES to detect humidity changes.

(B) The output voltage of WW-TES.

(C) The mechanism of the humidity effect on WW-TES.

as shown in Figure 5G. From this result, it is also possible to differentiate between signals during tremor and without tremor. The stability of the WW-TES was further evaluated through continuous operation for 72 h (1st round), followed by storage under ambient conditions before an additional uninterrupted 72-h test (2nd round). Comparative results, as illustrated in Figure S4 of the supporting information, indicate that the WW-TES maintained a highly stable electrical output signal. Even under a 7 Hz applied force, the output voltage showed no significant decrease over the two rounds of 72-h continuous operation.

SEM images in Figures S5A and S5B present the comparison of surface morphology for roughness PTFE before and after prolonged uses. The rough surface with clear groove lines can be seen due to the polishing with sandpaper. After prolonged use for 144 h, some rough spots were smoothed out due to long contact with the oscillating plate but keep showing grooves. Scratches on the PTFE surface are still evident, which means that initial features of the surface still remain after extended operation. The AFM images of the PTFE surface post-stability testing, shown in Figures S5C and S5D, reveal a roughness (S_q) of approximately 206 nm, which is only marginally lower than the initial S_q of modified PTFE (~228 nm) prior to operation. These results confirm that the WW-TES device can operate continuously without degradation in electrical signal stability or material integrity. This stability can be attributed to the nature of the signal generation process, which relies solely on contact rather than applying substantial pressure between the PTFE and the oscillating plate.

The TES operation is dependent on surface phenomena, which means that external factors can have an impact on the corresponding electrical signal. Moisture (H_2O) in the air, along with other organic/inorganic contaminants, can pose a serious problem for the TES's function and operation. High humidity, in particular, can create a conductive layer that can act as a driving force for the accumulated charges to dissipate on the tribe material's surface, resulting in unreliable or incorrect data. To investigate the influence of humidity on the output voltage of the WW-TES, the device was continuously operated under various humidity levels ranging from low to high. Figure 6A presents a visual depiction of the experimental setup and the WW-TES operation to detect the change in the humidity conditions. According to the output voltage results in Figure 6B, the linear correlation of output voltage with the increasing humidity levels is illustrated. The WW-TES could exhibit the distinguishable AC voltage with the changing of humidity from 21 to 81% RH, where a significant decrease in output voltage was observed from almost 1.0 to 0.2 V Figure 6C displays the working mechanism of the effect of humidity on the output voltage of WW-TES. Indeed, the interaction of water molecules can be possibly addressed in two steps: (1) chemisorption of the first H_2O layer and (2) physisorption of the following H_2O layers. The electrical field generated along this triboelectrification and electrostatic

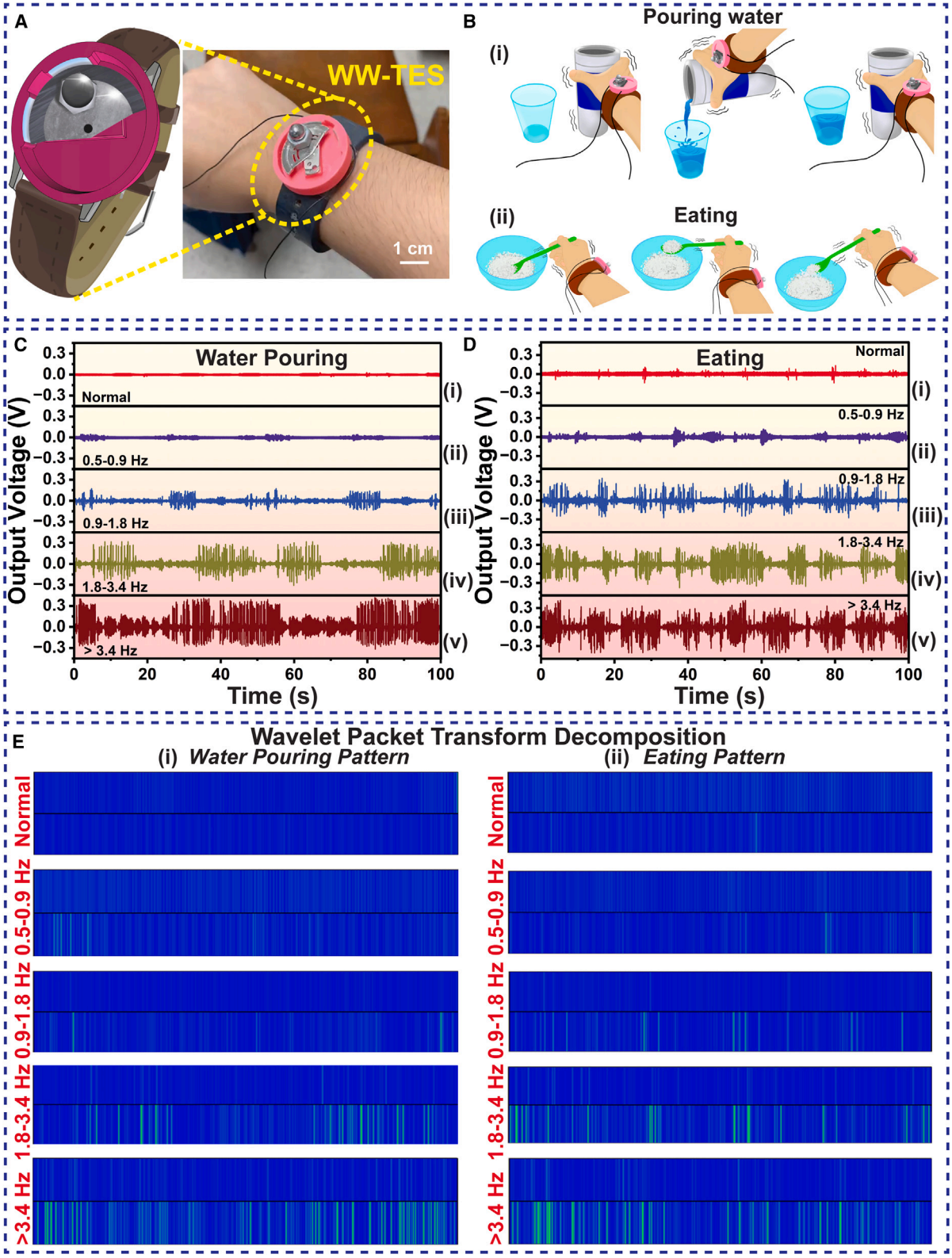

(legend on next page)

induction can lead to protons (H^+) hopping among the surface-absorbed H_2O and provide the hydroxide (OH^-) and hydronium (H_3O^+) species.[45] In the initial stage, at low humidity conditions (21%RH), chemisorption occurs as a small quantity of water molecules forms the initial layer on the triboelectric material surface at low relative humidity. The water molecules chemisorbed onto the surface of triboelectric materials and then undergo proton migration by hopping across the surface and making H_2O dissociation into H_3O^+ and OH^- following the equation of $H_2O + H_2O \rightarrow OH^- + H_3O^+$.[46] Due to the restriction of this layer by chemisorption, this process does not impact the resistance and may not change significantly the charge carrier density of the solid layer. When the humidity increases to the middle region of the RH level, a serial water layer can be formed. Other water molecules tend to be physisorpted on the surface of the first chemisorbed H_2O layer or even OH^- through hydrogen bonds. According to the Grotthuss explanation of the ion transfer mechanism, when the RH level is further increased, more and more water is adsorbed and reaches three or more layers of serial water molecules that accelerate the transfer of H^+, leading to the provision of more charge carriers.[47] Therefore, as humidity levels rise, the production of ions occurs, and their movement over energy barriers between these physiosorbed layers enables the hopping of protons through neighboring absorbed water molecules.[45] The additional charge flow would lead to leakage current during WW-TES operation and thus decrease the electrical output of the TES devices. The physique process is responsible for the notable drop in the voltage of the WW-TES between 21 and 81% RH. It is shown that the WW-TES should be operated and worked without high humidity or even not further kept in a high-humidity environment.

Practical application test

Tremors are a critical symptom in individuals with Parkinson's disease (PD). The severity of tremors often indicates the progression and severity of the disease. Currently, the tremor severity in PD is assessed on a scale of 0–4 based on the Movement Disorder Society-sponsored revision of the Unified Parkinson's Disease Rating Scale (MDS-UPDRS) scale.[48,49] The scale categorizes the disease based on the frequency of tremors. Level 0 represents the absence of symptoms or normal functioning, while level 1 shows slight, low-frequency tremors (0.5–0.9 Hz) with minimal impact on function. Symptoms or signs of such low frequency or intensity do not affect functionality. Level 2 represents mild tremors at a frequency of 0.9–1.8 Hz, resulting in modest functional disruption and a noticeable impact on daily life. Level 3 signifies moderate tremors occurring at a frequency of 1.8–3.4 Hz, significantly affecting function without preventing it. As a result, individuals may experience challenges with activities of daily living such as dressing, eating, and writing. Level 4 denotes severe tremors exceeding 3.4 Hz, resulting in symptoms or signs that severely impair normal function. These very severe symptoms profoundly affect daily life, leading to substantial limitations in activities of daily living, significant loss of independence, and a severe impact on quality of life. The MDS-UPDRS scale is a standardized tool used by clinicians and researchers to evaluate the severity and progression of Parkinson's disease symptoms. It helps clinicians monitor disease progression, assess the effectiveness of treatment, and make informed decisions about patient care.[50]

In order to test the effectiveness of the WW-TES device in monitoring Parkinson's disease in real-time, the device is secured with a strap and worn on the wrist like a watch. This is shown in Figure 7A. The test involves simulating tremors associated with varying levels of PD severity by performing everyday tasks, known as activities of daily living (ADLs).[51] The MDS-UPDRS ADL section is used to assess an individual's ability to perform daily personal tasks including bathing, dressing, eating, and pouring liquids.[52] Difficulties in performing these activities can significantly impact the independence and quality of life of individuals with Parkinson's disease (PD). Therefore, this study, evaluated the proficiency of individuals with PD in handling utensils by conducting ADL tasks such as eating and pouring water. These tasks provide valuable insights into an overall motor symptoms of the individual. For the water-pouring activity, the sequence of movements included picking up a container, lifting it, pouring water into a glass, and setting the container back down. This sequence simulates the process of pouring water from a container into a glass, as depicted in Figure 7B (i). Similarly, for the eating activity, the movements involved lifting a spoon, scooping food upwards, and alternating the position of spoon between up and down, mimicking typical actions during eating, as illustrated in Figure 7B (ii). Throughout both activities, the WW-TES device was worn on the wrist. The tremor intensity was adjusted according to the frequency levels specified by the MDS-UPDRS scale, which measures the severity of Parkinson's disease (PD) tremors.

To capture the electrical output data, the WW-TES device was connected to a NodeMCU ESP8266, which features a Wi-Fi module for IoT integration. The connection diagram is presented in Figure S6 of the supplementary information. The NodeMCU ESP8266 includes one analog pin (A0), 16 digital pins, three 3.3 V power pins, and four GND pins. The electrical signal from the WW-TES is directed to the A0 pin, with the device output linked to the A0 and GND pins on the NodeMCU ESP8266. This configuration enables the ESP8266 to display real-time data on a computer screen or store the recorded data for further analysis by experts.

The output signal presented in Figure 7C (i) shows the output signal for the 28activity of pouring water, capturing movements of both a normal state (no tremor) and tremor occurrence during the task. During the normal state, the wearer could lift the container and pour water into a glass without any trouble due to the absence of hand shaking. Without hand shaking, there is

Figure 7. Practical application: Activities of daily living (ADLs) testing

(A) Schematic image of WW-TES device in this work (the scale bar is 1 cm)

(B) Schematic of activity movement for the experiment: (i) pouring water and (ii) eating.

(C) Output signal for water pouring activity.

(D) Output signal for eating activity (E) Wavelet packet transform decomposition: (i) water pouring, and (ii) eating.

no mechanical force to trigger the rotor plate inside the device to rotate, resulting in no output signal being generated. However, there are noticeable peaks in the output signal due to the wrist movement when picking up the container and pouring water. This hand movement causes the rotor plate to rotate against the PTFE plate, resulting in a small electrical peak output. On the contrary, when the frequency of the tremor increased, the WW-TES device produced output signals directly proportional to the tremor frequency intensity. According to Figure 7C (ii-v), two regions of the signal were observed which are higher amplitude and lower amplitude in one output signal. The higher amplitude region is indicated when picking up and holding the container, while the lower amplitude region is for the turning of the wrist to pour water into a glass with the shaking hand. Similar to output signals have been observed from eating experiments. In Figure 7D (i), the normal state is depicted, where no peak output is generated due to the absence of hand tremors. However, some peak outputs appear, attributed to hand movements while scooping rice, causing the rotor plate to be able to rotate against PTFE films and generate small peak signals. On the other hand, as the tremor frequency increases, the output signal also increases as can be seen in Figure 7D (ii-v). During eating movements with hand tremors, the output signal shows two distinct regions: a lower amplitude region during spoon lifting and rice scooping, and a higher amplitude region when trying to hold up the spoon. The results of the two activities have shown that as the frequency increases, the output signal amplitude also increases proportionally with the tremor frequency level 0–4 of the MDS-UPDRS scale. This indicates that the WW-TES device can detect the severity of Parkinson's disease, indicating whether it has progressed or not. Electrical signals can reveal if the severity is increasing as more intense tremors result in higher electrical output signals. Early clinical identification of PD is crucial to stop the disease from progressing. In this regard, we provide effective approaches for impacted person detection based on wavelet packet transforms (WPT). For detection, the signals are first preprocessed, and patterns are produced using the WPT. Two distinct instances for different people are taken into consideration when they eat and pour water. Two distinct impulses are obtained using the WW-TES in this proposed work. The output signals from the device are gathered and supplied into the WPT. The contours show that the color coding in WPT changes for an affected individual and a normal one, which aids in determining whether to seek medical assistance. Figure 7E illustrates how WPT is used to detect the movement of the pouring of water pouring event and eating, respectively. The ability of the WW-TES to capture vibration patterns throughout the day offers valuable insights into a patient's PD tremor characteristics. This continuous data stream can be leveraged for enhanced disease monitoring, as tracking changes in vibration patterns over time can provide a more objective understanding of disease progression and treatment efficacy. Integrating WW-TES data with large datasets of Parkinson's patient vibration patterns could pave the way for the development of computational algorithms for predicting disease severity, symptom exacerbation, and potentially, treatment response. This approach holds promise for transitioning PD management from a reactive to a predictive model, enabling personalized treatment strategies and improved patient outcomes. Although various PD sensors utilizing different technologies are available on both commercial and laboratory scales, the WW-TES offers distinct advantages for future development. Its design leverages simple materials, a straightforward fabrication process, and cost-effectiveness, making it a promising option for PD tremor detection. A comparison of PD sensors employing other technologies, detailing their structure, type, detection method, operating frequency, device size, scale, and limitations, is provided in the supplementary information (Table S2).

Conclusions

This work presents a wristwatch-integrated triboelectric sensor (WW-TES) for continuous and unobtrusive tremor monitoring in Parkinson's disease (PD). The WW-TES design leverages a free-standing triboelectric mechanism with optimized electrode distance, demonstrating a direct correlation between tremor severity (based on MDS-UPDRS) and the captured signal amplitude during activities of daily living. This finding suggests the potential of WW-TES as a tool for objective tremor assessment and early detection of severe PD symptoms. Furthermore, the self-powered nature of the sensor paves the way for integration with real-time monitoring systems and tremor prediction algorithms. Future studies will explore the long-term performance of the WW-TES in clinical settings and its potential for personalized treatment strategies in PD management.

Limitations of the study

So far, the prototype of the WW-TES has been tested only in lab simulations; the clinical trials with patients with PD will follow pending the approvals from regulators. Currently, the device requires wired connections, hence impacts portability and comfort. Integration with NodeMCU ESP8266 is foreseen in order to implement a wireless version. Real-time feedback for both the patient and the provider cannot be provided in the present state of development, but this will be added in subsequent versions with a view to further extending the monitoring capability. Initial long-term stability testing under controlled conditions has been promising, but additional studies are required to determine durability for everyday use.

RESOURCE AVAILABILITY

Lead contact

Further information and requests for resources and reagents should be directed to and will be fulfilled by the Lead Contact, Naratip Vittayakorn (naratip.vi@kmitl.ac.th).

Materials availability

Materials used in the study are commercially available.

Data and code availability

- Data: all data reported in this article is available from the lead contacts upon reasonable request. Data supporting the findings presented can be found within the body of the article and the supplemental information.
- Code: No new code was developed for this study.
- Other items: Additional information needed to reanalyze the data presented in this article can be obtained from the lead contacts upon reasonable request.

ACKNOWLEDGMENTS

This work was supported financially by the Thailand Science Research and Innovation (TSRI), Ministry of Higher Education and Science, Research and Innovation (MHESI), Thailand, Thailand Institute of Nuclear Technology (FFB660061/0255) and Srinakharinwirot University (Grant 471/2567). Moreover, this work is partially supported by the National Research Foundation of Korea (RS-2024-00346135, RS-2024-00431411).

AUTHOR CONTRIBUTIONS

S. Ukasi: Methodology, investigation, and writing – original draft. **S. Pongampai:** Methodology. **B. K. Panigrahi:** Formal analysis. **S. Panda:** Methodology and writing – original draft. **S. Hajra:** Methodology and writing – original draft. **H. J. Kim:** Resources and writing – review and editing. **N. Vittayakorn:** Conceptualization writing – review and editing, supervision, funding acquisition, and project administration. **T. Charoonsuk:** Conceptualization, writing – original draft, writing – review and editing, supervision, funding acquisition, and project administration.

DECLARATION OF INTERESTS

The authors declare no competing interests.

STAR★METHODS

Detailed methods are provided in the online version of this paper and include the following:

- KEY RESOURCES TABLE
- EXPERIMENTAL MODEL AND SUBJECT DETAILS
- METHOD DETAILS
  - Materials preparation
  - Characterizations
  - Regular TES fabrication
  - Electrical output measurement and signal analysis
- QUANTIFICATION AND STATISTICAL ANALYSIS
- ADDITIONAL RESOURCES

SUPPLEMENTAL INFORMATION

Supplemental information can be found online at https://doi.org/10.1016/j.isci.2024.111480.

Received: May 24, 2024
Revised: October 23, 2024
Accepted: November 22, 2024
Published: November 26, 2024

REFERENCES

1. Bhidayasiri, R., Kalia, L.V., and Bloem, B.R. (2023). Tackling Parkinson's Disease as a Global Challenge. J. Parkinsons Dis. *13*, 1277–1280. https://doi.org/10.3233/jpd-239005.
2. Isaacson, S.H., and Hauser, R.A. (2009). Improving symptom control in early Parkinson's disease. Ther. Adv. Neurol. Disord. *2*, 29–41. https://doi.org/10.1177/1756285609339383.
3. Adams, J.L., Dinesh, K., Snyder, C.W., Xiong, M., Tarolli, C.G., Sharma, S., Dorsey, E.R., and Sharma, G. (2021). A real-world study of wearable sensors in Parkinson's disease. NPJ Parkinsons Dis. *7*, 106. https://doi.org/10.1038/s41531-021-00248-w.
4. Davidashvilly, S., Cardei, M., Hssayeni, M., Chi, C., and Ghoraani, B. (2024). Deep neural networks for wearable sensor-based activity recognition in Parkinson's disease: investigating generalizability and model complexity. Biomed. Eng. Online *23*, 17. https://doi.org/10.1186/s12938-024-01214-2.
5. Burkhard, P.R., Shale, H., Langston, J.W., and Tetrud, J.W. (1999). Quantification of dyskinesia in Parkinson's disease: Validation of a novel instrumental method. Mov. Disord. *14*, 754–763. https://doi.org/10.1002/1531-8257.
6. Rabelo, A.G., Neves, L.P., Paixão, A.P.S., Oliveira, F.H.M., de Souza, L.A.P.S., Vieira, M.F., Pereira, A.A., and Andrade, A.O. (2017). Objective Assessment of Bradykinesia Estimated from the Wrist Extension in Older Adults and Patients with Parkinson's Disease. Ann. Biomed. Eng. *45*, 2614–2625. https://doi.org/10.1007/s10439-017-1908-3.
7. Ukasi, S., Jutapukti, P., Ninthub, C., Pinpru, N., Pakawanit, P., Vittayakorn, W., Pongampai, S., Vittayakorn, N., and Charoonsuk, T. (2024). Gamma glycine enhances efficiency of organic hybrid piezoelectric-triboelectric nanogenerators. Nano Energy *119*, 109045. https://doi.org/10.1016/j.nanoen.2023.109045.
8. Kim, H.-G., Hajra, S., Lee, H., Kim, N., and Kim, H.J. (2023). Additively Manufactured Mechanical Metamaterial-Based Pressure Sensor with Tunable Sensing Properties for Stance and Motion Analysis. Adv. Eng. Mater. *25*, 2201499. https://doi.org/10.1002/adem.202201499.
9. Zhang, H., Zhang, X., Qiu, C., Jia, P., An, F., Zhou, L., Zhu, L., and Zhang, D. (2024). Polyaniline/ZnO heterostructure-based ammonia sensor self-powered by electrospinning of PTFE-PVDF/MXene piezo-tribo hybrid nanogenerator. Chem. Eng. J. *496*, 154226. https://doi.org/10.1016/j.cej.2024.154226.
10. Song, H., Panda, S., Hajra, S., Hwang, S., Jo, J., Kim, N., Panigrahi, B.K., Yu, J., Jeong, S.M., and Kim, H.J. (2024). A Self-Powered Smart White Cane for Improving Mobility of Visually Impaired Person Using a Triboelectric Nanogenerator. Energ. Tech. *12*, 2400424. https://doi.org/10.1002/ente.202400424.
11. Li, Q., Dai, K., Zhang, W., Wang, X., You, Z., and Zhang, H. (2021). Triboelectric nanogenerator-based wearable electronic devices and systems: Toward informatization and intelligence. Digit. Signal Process. *113*, 103038. https://doi.org/10.1016/j.dsp.2021.103038.
12. Pu, X., Zhang, C., and Wang, Z.L. (2023). Triboelectric nanogenerators as wearable power sources and self-powered sensors. Natl. Sci. Rev. *10*, nwac170. https://doi.org/10.1093/nsr/nwac170.
13. Zhang, H., Zhang, D., Yang, Y., Zhou, L., Liu, Y., Liu, W., Sun, Y., Guo, Y., and Ji, Y. (2024). Eco-friendly triboelectric nanogenerator for self-powering stacked In2O3 nanosheets/PPy nanoparticles-based NO2 gas sensor. Nano Energy *128*, 109978. https://doi.org/10.1016/j.nanoen.2024.109978.
14. Zhang, H., Chen, X., Liu, Y., Yang, C., Liu, W., Qi, M., and Zhang, D. (2024). PDMS Film-Based Flexible Pressure Sensor Array with Surface Protruding Structure for Human Motion Detection and Wrist Posture Recognition. ACS Appl. Mater. Interfaces *16*, 2554–2563. https://doi.org/10.1021/acsami.3c14036.
15. Zhang, H., Zhang, D.-Z., Wang, D.-Y., Xu, Z.-Y., Yang, Y., and Zhang, B. (2022). Flexible single-electrode triboelectric nanogenerator with MWCNT/PDMS composite film for environmental energy harvesting and human motion monitoring. Rare Met. *41*, 3117–3128. https://doi.org/10.1007/s12598-022-02031-z.
16. Zhang, H., Zhang, D., Mao, R., Zhou, L., Yang, C., Wu, Y., Liu, Y., and Ji, Y. (2024). MoS2-based charge trapping layer enabled triboelectric nanogenerator with assistance of CNN-GRU model for intelligent perception. Nano Energy *127*, 109753. https://doi.org/10.1016/j.nanoen.2024.109753.
17. Kim, N., Hwang, S., Panda, S., Hajra, S., Jo, J., Song, H., Belal, M.A., Vivekananthan, V., Panigrahi, B.K., Achary, P.G.R., and Kim, H.J. (2024). A Sustainable Free-Standing Triboelectric Nanogenerator Made of Flexible Composite Film for Brake Pattern Recognition in Automobiles. Macromol. Rapid Commun. *45*, 2400431. https://doi.org/10.1002/marc.202400431.
18. Shao, B., Lu, M.-H., Wu, T.-C., Peng, W.-C., Ko, T.-Y., Hsiao, Y.-C., Chen, J.-Y., Sun, B., Liu, R., and Lai, Y.-C. (2024). Large-area, untethered, metamorphic, and omnidirectionally stretchable multiplexing self-powered triboelectric skins. Nat. Commun. *15*, 1238. https://doi.org/10.1038/s41467-024-45611-6.

19. Liu, Y., Shen, Y., Ding, W., Zhang, X., Tian, W., Yang, S., Hui, B., and Zhang, K. (2023). All-natural phyllosilicate-polysaccharide triboelectric sensor for machine learning-assisted human motion prediction. npj Flex. Electron. *7*, 21. https://doi.org/10.1038/s41528-023-00254-3.

20. Zhang, H., Zhang, D., Guan, J., Wang, D., Tang, M., Ma, Y., and Xia, H. (2022). A flexible wearable strain sensor for human-motion detection and a human–machine interface. J. Mater. Chem. C Mater. *10*, 15554–15564. https://doi.org/10.1039/D2TC03147G.

21. Gao, M., Yang, Z., Choi, J., Wang, C., Dai, G., and Yang, J. (2024). Triboelectric Nanogenerators for Preventive Health Monitoring. Nanomaterials *14*, 336. https://doi.org/10.3390/nano14040336.

22. Mao, J., Zhou, P., Wang, X., Yao, H., Liang, L., Zhao, Y., Zhang, J., Ban, D., and Zheng, H. (2023). A health monitoring system based on flexible triboelectric sensors for intelligence medical internet of things and its applications in virtual reality. Nano Energy *118*, 108984. https://doi.org/10.1016/j.nanoen.2023.108984.

23. Zhu, M., Shi, Q., He, T., Yi, Z., Ma, Y., Yang, B., Chen, T., and Lee, C. (2019). Self-Powered and Self-Functional Cotton Sock Using Piezoelectric and Triboelectric Hybrid Mechanism for Healthcare and Sports Monitoring. ACS Nano *13*, 1940–1952. https://doi.org/10.1021/acsnano.8b08329.

24. Liu, G., Liu, R., Guo, H., Xi, Y., Wei, D., and Hu, C. (2016). A Novel Triboelectric Generator Based on the Combination of a Waterwheel-Like Electrode with a Spring Steel Plate For Efficient Harvesting of Low-Velocity Rotational Motion Energy. Adv. Electron. Mater. *2*, 1500448. https://doi.org/10.1002/aelm.201500448.

25. Vera Anaya, D., and Yuce, M.R. (2021). Stretchable triboelectric sensor for measurement of the forearm muscles movements and fingers motion for Parkinson's disease assessment and assisting technologies. Med. Devices Sens. *4*, e10154. https://doi.org/10.1002/mds3.10154.

26. Kim, J.-N., Lee, J., Lee, H., and Oh, I.-K. (2021). Stretchable and self-healable catechol-chitosan-diatom hydrogel for triboelectric generator and self-powered tremor sensor targeting at Parkinson disease. Nano Energy *82*, 105705. https://doi.org/10.1016/j.nanoen.2020.105705.

27. Zhao, Z., Zhou, L., Li, S., Liu, D., Li, Y., Gao, Y., Liu, Y., Dai, Y., Wang, J., and Wang, Z.L. (2021). Selection rules of triboelectric materials for direct-current triboelectric nanogenerator. Nat. Commun. *12*, 4686. https://doi.org/10.1038/s41467-021-25046-z.

28. Charoonsuk, T., Muanghlua, R., Sriphan, S., Pongampai, S., and Vittayakorn, N. (2021). Utilization of commodity thermoplastic polyethylene (PE) by enhanced sensing performance with liquid phase electrolyte for a flexible and transparent triboelectric tactile sensor. Sustainable Materials and Technologies *27*, e00239. https://doi.org/10.1016/j.susmat.2020.e00239.

29. Charoonsuk, T., Supansomboon, S., Pakawanit, P., Vittayakorn, W., Pongampai, S., Woramongkolchai, S., and Vittayakorn, N. (2022). Simple enhanced charge density of chitosan film by the embedded ion method for the flexible triboelectric nanogenerator. Carbohydr. Polym. *297*, 120070. https://doi.org/10.1016/j.carbpol.2022.120070.

30. Pharino, U., Sinsanong, Y., Pongampai, S., Charoonsuk, T., Pakawanit, P., Sriphan, S., Vittayakorn, N., and Vittayakorn, W. (2021). Influence of pore morphologies on the mechanical and tribo-electrical performance of polydimethylsiloxane sponge fabricated via commercial seasoning templates. Radiat. Phys. Chem. *189*, 109720. https://doi.org/10.1016/j.radphyschem.2021.109720.

31. Pongampai, S., Pakawanit, P., Charoonsuk, T., Hajra, S., Kim, H.J., and Vittayakorn, N. (2023). Design and optimization of Miura-Origami-inspired structure for high-performance self-charging hybrid nanogenerator. J. Sci.: Advanced Materials and Devices *8*, 100618. https://doi.org/10.1016/j.jsamd.2023.100618.

32. Niu, S., Liu, Y., Chen, X., Wang, S., Zhou, Y.S., Lin, L., Xie, Y., and Wang, Z.L. (2015). Theory of freestanding triboelectric-layer-based nanogenerators. Nano Energy *12*, 760–774. https://doi.org/10.1016/j.nanoen.2015.01.013.

33. Prada, T., Harnchana, V., Lakhonchai, A., Chingsungnoen, A., Poolcharuansin, P., Chanlek, N., Klamchuen, A., Thongbai, P., and Amornkitbamrung, V. (2022). Enhancement of output power density in a modified polytetrafluoroethylene surface using a sequential O2/Ar plasma etching for triboelectric nanogenerator applications. Nano Res. *15*, 272–279. https://doi.org/10.1007/s12274-021-3470-4.

34. Wang, X., Niu, S., Yin, Y., Yi, F., You, Z., and Wang, Z.L. (2015). Triboelectric Nanogenerator Based on Fully Enclosed Rolling Spherical Structure for Harvesting Low-Frequency Water Wave Energy. Adv. Energy Mater. *5*, 1501467. https://doi.org/10.1002/aenm.201501467.

35. Zhang, Z., Hu, Z., Wang, Y., Wang, Y., Zhang, Q., Liu, D., Wang, H., and Xu, M. (2022). Multi-Tunnel Triboelectric Nanogenerator for Scavenging Mechanical Energy in Marine Floating Bodies. J. Mar. Sci. Eng. *10*, 455. https://doi.org/10.3390/jmse10040455.

36. Guo, X., Li, F., Xi, Z., Hong, J., Wang, Y., Qian, Z., Yu, H., Zhu, C., Du, H., Si, J., et al. (2024). Boosting Free-Rotating Disk Triboelectric Nanogenerator through Alcohol-Soluble Nylon Film, Preventing Air Breakdown. ACS Appl. Electron. Mater. *6*, 376–385. https://doi.org/10.1021/acsaelm.3c01381.

37. Fu, J., Xia, X., Xu, G., Li, X., and Zi, Y. (2019). On the Maximal Output Energy Density of Nanogenerators. ACS Nano *13*, 13257–13263. https://doi.org/10.1021/acsnano.9b06272.

38. Song, W.-Z., Qiu, H.-J., Zhang, J., Yu, M., Ramakrishna, S., Wang, Z.L., and Long, Y.-Z. (2021). Sliding mode direct current triboelectric nanogenerators. Nano Energy *90*, 106531. https://doi.org/10.1016/j.nanoen.2021.106531.

39. Zi, Y., Wu, C., Ding, W., and Wang, Z.L. (2017). Maximized Effective Energy Output of Contact-Separation-Triggered Triboelectric Nanogenerators as Limited by Air Breakdown. Adv. Funct. Mater. *27*, 1700049. https://doi.org/10.1002/adfm.201700049.

40. Zurbuchen, A., Pfenniger, A., Stahel, A., Stoeck, C.T., Vandenberghe, S., Koch, V.M., and Vogel, R. (2013). Energy Harvesting from the Beating Heart by a Mass Imbalance Oscillation Generator. Ann. Biomed. Eng. *41*, 131–141. https://doi.org/10.1007/s10439-012-0623-3.

41. Onwudili, A.E., and Iweka, S.C. (2021). Full-annealing and its effect on the Mechanical Properties of Alloy 304H Stainless Steel. Journal of Engineering Research and Reports *20*, 28–44. https://doi.org/10.9734/jerr/2021/v20i717339.

42. Calle, L., MacDowell, L., and Vinje, R. (2004). Electrochemical Evaluation of Stainless Steels in Acidic Sodium Chloride Solutions. In NACE CORROSION (NACE), pp. NACE04303.

43. Jahnke, T., Hergenhahn, U., Winter, B., Dörner, R., Frühling, U., Demekhin, P.V., Gokhberg, K., Cederbaum, L.S., Ehresmann, A., Knie, A., and Dreuw, A. (2020). Interatomic and Intermolecular Coulombic Decay. Chem. Rev. *120*, 11295–11369. https://doi.org/10.1021/acs.chemrev.0c00106.

44. Chan, P.Y., Ripin, Z.M., Halim, S.A., Arifin, W.N., Yahya, A.S., Eow, G.B., Tan, K., Hor, J.Y., and Wong, C.K. (2022). Motion characteristics of subclinical tremors in Parkinson's disease and normal subjects. Sci. Rep. *12*, 4021. https://doi.org/10.1038/s41598-022-07957-z.

45. Mohamadbeigi, N., Shooshtari, L., Fardindoost, S., Vafaiee, M., Iraji zad, A., and Mohammadpour, R. (2024). Self-powered triboelectric nanogenerator sensor for detecting humidity level and monitoring ethanol variation in a simulated exhalation environment. Sci. Rep. *14*, 1562. https://doi.org/10.1038/s41598-024-51862-6.

46. Sardana, S., Singh, Z., Sharma, A.K., Kaur, N., Pati, P.K., and Mahajan, A. (2022). Self-powered biocompatible humidity sensor based on an electrospun anisotropic triboelectric nanogenerator for non-invasive diagnostic applications. Sensor. Actuator. B Chem. *371*, 132507. https://doi.org/10.1016/j.snb.2022.132507.

47. Panda, S., Jeong, H., Hajra, S., Rajaitha, P.M., Hong, S., and Kim, H.J. (2023). Biocompatible polydopamine based triboelectric nanogenerator for humidity sensing. Sensor. Actuator. B Chem. *394*, 134384. https://doi.org/10.1016/j.snb.2023.134384.

48. AlMahadin, G., Lotfi, A., Carthy, M.M., and Breedon, P. (2021). Enhanced Parkinson's Disease Tremor Severity Classification by Combining Signal Processing with Resampling Techniques. SN Computer Science *3*, 63. https://doi.org/10.1007/s42979-021-00953-6.

49. Goetz, C.G., Tilley, B.C., Shaftman, S.R., Stebbins, G.T., Fahn, S., Martinez-Martin, P., Poewe, W., Sampaio, C., Stern, M.B., Dodel, R., et al. (2008). Movement Disorder Society-sponsored revision of the Unified Parkinson's Disease Rating Scale (MDS-UPDRS): Scale presentation and clinimetric testing results. Mov. Disord. *23*, 2129–2170. https://doi.org/10.1002/mds.22340.

50. Regnault, A., Boroojerdi, B., Meunier, J., Bani, M., Morel, T., and Cano, S. (2019). Does the MDS-UPDRS provide the precision to assess progression in early Parkinson's disease? Learnings from the Parkinson's progression marker initiative cohort. J. Neurol. *266*, 1927–1936. https://doi.org/10.1007/s00415-019-09348-3.

51. Seichepine, D.R., Neargarder, S., Miller, I.N., Riedel, T.M., Gilmore, G.C., and Cronin-Golomb, A. (2011). Relation of Parkinson's Disease Subtypes to Visual Activities of Daily Living. J. Int. Neuropsychol. Soc. *17*, 841–852. https://doi.org/10.1017/S1355617711000853.

52. Shulman, L.M., Pretzer-Aboff, I., Anderson, K.E., Stevenson, R., Vaughan, C.G., Gruber-Baldini, A.L., Reich, S.G., and Weiner, W.J. (2006). Subjective report versus objective measurement of activities of daily living in Parkinson's disease. Mov. Disord. *21*, 794–799. https://doi.org/10.1002/mds.20803.

STAR★METHODS

KEY RESOURCES TABLE

REAGENT or RESOURCE	SOURCE	IDENTIFIER
Software and algorithms		
Origin 2024b	OriginLab	N/A
DMM Viewer2	GW Instek	N/A
Shapr3D APP	Shapr3D	N/A
ideasMaker 4.3.2 Raise3D E2	ideasmaker.net	N/A
Other		
Stainless steel rotor	Commercial Supplier	N/A
stainless-steel plate grade SUS304	Commercial Supplier	N/A
PTFE	Commercial Supplier	N/A
Aluminum tape	Commercial Supplier	N/A
30AWG wire	Commercial Supplier	N/A
PLA filament	Commercial Supplier	N/A

EXPERIMENTAL MODEL AND SUBJECT DETAILS

This research involved test subjects wearing watch sensors tasked to evaluate the detection of the tremor and generate output signals. In this study, the researcher is the subject in simulating Parkinson's disease tremors from mild to very severe. These simulations are based on the MDS-UPDRS scale-a rating system that classifies the tremors by frequency, and hence the obtained signals were analyzed.

METHOD DETAILS

Materials preparation

A commercial stainless-steel plate grade SUS304 (Guenter Company, Thailand) with 0.5 mm in thickness was used as tribo-positive material. The PTFE film with 0.1 mm in thickness was selected as tribo-negative material. The surface-modified PTFE was done through polishing using sandpaper number 1,000 and polished in a unidirectional manner with a specified cycle of 2 times, resulting in the creation of a roughened PTFE surface. Both commercial stainless-steel and surface-modified PTFE film were cut into 2 × 2 cm^2 for the regular TES device. The commercial stainless-steel rotor plate was used instead of stainless-steel film to fabricate the WW-TES by following the custom design. Polylactic acid (PLA) filament (purchased from Shenzhen eSUN Industrial Co; Ltd) was used in 3D printing. With the exception of PTFE, all the materials were used as received.

Characterizations

The morphological and surface roughness characteristics of PTFE were investigated using Scanning Electron Microscopy (SEM; FEI QUANTA 250) with the secondary electron detector at accelerating voltages of 20 kV. Additionally, high-resolution Atomic Force Microscopy (AFM) (Seiko Instruments SPI3800N/SPA400) was conducted in Dynamic Force Mode (DFM), also known as tapping mode, with a 20 μm scanner. Silicon cantilevers covered with a thin reflex aluminum coating, featuring nominal spring constants (k) ranging from 36 to 90 N/m and resonance frequencies of 160–225 kHz, were employed. The Attenuated Total Reflection-Infrared Spectroscopy (ATR-IR; Shimadzu IRTracer-100) was employed to identify the functional groups of PTFE in the range of ATR-IR spectrum within 4000-550 cm^{-1}. Energy Dispersive X-ray Spectroscopy (EDS; Bruker) was used to analyze the elemental composition of the rotor plate to confirm its stainless-steel composition.

Regular TES fabrication

The TES device comprises a pair of triboelectric materials in an FS mode structure. Firstly, a 2 × 2 cm^2 PTFE film is cut, and an Al tape of the same size is attached to its one side to act as an electrode. This electrode is then connected to an electrical wire. On the other side of the device, a stainless-steel film of the same size is cut and connected to the electrical wire.

Electrical output measurement and signal analysis

The study focuses on the electrical output performance of a TES device, which is divided into two parts. In the first part, the electrical output of the basic TES device was measured under compressive force using a sliding testing machine that moves horizontally back and forth. The V_{OC} and I_{SC} signals were measured using a Digital Storage Oscilloscope (Keysight DSO-X 2012A) and Digital Multimeter (DMM; GDM-9061 Dual Measurement Multimeter). The frequency can be adjusted to study the electrical output characteristics by controlling the speed of the motor of a sliding testing machine. In the second part, the output performance of the WW-TES device was measured for the PD monitoring application. For testing the WW-TES, an orbital shaker was employed to provide vibrational forces during electrical output measurements. The shaker's adjustable frequency range allowed for tests within the Parkinson's tremor frequency range (3–7 Hz), enabling a simulation that closely resembles real-life operating conditions for the sensor. In all measurement conditions, electric wires were connected directly from the device to an oscilloscope and a digital multimeter (DMM) to record voltage and current, respectively.

The application of the WW-TES for Parkinson's tremor detection was evaluated through simulated scenarios. A typical patient activity was mimicked by adjusting hand-shaking frequency according to each symptom level, with the WW-TES worn throughout. After acquiring the electrical signal data, tremor pattern analyses were conducted using MATLAB R2016a software, utilizing the third decomposition level of the Daubechies wavelet transform for accurate pattern recognition.

QUANTIFICATION AND STATISTICAL ANALYSIS

The electrical output voltage and current were collected with oscilloscpe and digital multimeter (DMM). For practical application, the WW-TES data were colltect via NodeMCU ESP8266. Figures were produced by Origin from the raw data.

ADDITIONAL RESOURCES

This study has not generated or contributed to a new website/forum.